

Non-hydrostatic modelling of infragravity waves under laboratory conditions



Dirk P. Rijnsdorp*, Pieter B. Smit, Marcel Zijlema

Environmental Fluid Mechanics Section, Faculty of Civil Engineering and Geosciences, Delft University of Technology, P.O. Box 5048, 2600 GA, Delft, The Netherlands

ARTICLE INFO

Article history:

Received 16 August 2013

Received in revised form 18 November 2013

Accepted 22 November 2013

Available online 27 December 2013

Keywords:

Infragravity waves

Nonlinear interactions

Non-hydrostatic

Wave model

SWASH

ABSTRACT

The non-hydrostatic wave model SWASH is compared to flume observations of infragravity waves propagating over a plane slope and barred beach. The experiments cover a range of infragravity wave conditions, including forcing by bichromatic and irregular waves, varying from strongly dissipative to strongly reflective, so that model performance can be assessed for a wide range of conditions. The predicted bulk wave parameters, such as wave height and mean wave period, are found to be in good agreement with the observations. Moreover, the model captures the observed breaking of infragravity waves. These results demonstrate that SWASH can be used to model the nearshore evolution of infragravity waves, including nonlinear interactions, dissipation and shoreline reflections.

© 2013 Elsevier B.V. All rights reserved.

1. Introduction

As short-wave groups propagate towards the shore they force longer waves with periods ranging from 20 s to 250 s. Such low-frequency motions are commonly referred to as infragravity waves (ig-waves). IG-waves are found to be significant for harbour resonance (e.g. Bowers, 1977), moored vessel motions (e.g. Naciri et al., 2004), collapse of ice shelves (Bromirski et al., 2010) and dune erosion (e.g. van Thiel de Vries et al., 2008), which makes them an important subject for coastal and harbour engineers.

Two main mechanisms for the generation of ig-waves have been identified. Longuet-Higgins and Stewart (1962, 1964) proposed that groups of short waves force ig-waves through spatial gradients in the radiation stress. These ig-waves propagate with the velocity of the short-wave envelope and are known as bound ig-waves. Furthermore, Symonds et al. (1982) showed that the time variation of the breakpoint, induced by short-wave groups, generates a shoreward and seaward directed free ig-wave which propagate with the free wave celerity. The cross-shore propagation of ig-waves over an uneven bottom has been studied extensively by means of field experiments, laboratory experiments and numerical models. Such studies revealed that, as waves approach the shore, bound ig-waves grow with a rate greater than for energy conservative shoaling, due to weakly nonlinear interactions between short waves and bound ig-waves (e.g. Battjes et al., 2004; Janssen et al., 2003; List, 1992; Masselink, 1995). In the

nearshore, because ig-waves are generally much longer than the short waves which generate them, ig-waves can lose energy due to bottom friction (Henderson and Bowen, 2002). This is particularly important in case of an extensive flat and shallow region, such as a coral reef (Pomeroy et al., 2012), but less significant on sloping beaches (e.g. Henderson et al., 2006; Van Dongeren et al., 2007). Once ig-waves enter the surf zone, the wave motion becomes strongly nonlinear, energy is exchanged rapidly between the short waves and the ig-waves (Henderson et al., 2006; Thomson et al., 2006) and strong dissipation can occur due to ig-wave breaking (Van Dongeren et al., 2007). Ruju et al. (2012) suggested that, based on a numerical study, nonlinear interactions are strongest in the outer surf zone, whereas – if it occurs – ig-wave breaking appears to be the dominant process in the inner surf zone. For weakly dissipative conditions, ig-waves (partially) reflect at the beach and subsequently propagate in seaward direction. Because the short-wave motion is mostly destroyed in the surf zone, such seaward directed waves are free waves, which may either propagate towards deeper water, known as leaky waves, or become trapped in the coastal region by refraction, known as edge waves. The simultaneous presence of incoming, and outgoing ig-waves can result in a (partially) standing ig-wave pattern near the surf zone.

The large difference in scales and the various physical phenomena (e.g. friction, wave-breaking) involved in the evolution of ig-waves places stringent demands on numerical models. In the surf-zone, a full representation of the ig-wave dynamics not only involves resolving the wave groups, but also the individual waves, including small scale processes due to wave breaking. Resolving all relevant scales over relatively short temporal and spatial scales is now within reach of Reynolds-averaged Navier Stokes (RANS) type models (e.g. Lin and

* Corresponding author. Tel.: +31 15 278 5433.

E-mail address: d.p.rijnsdorp@tudelft.nl (D.P. Rijnsdorp).

Liu, 1998), as is exemplified by the successful application of such a model to simulate low-frequency motions under laboratory conditions (e.g. Lara et al., 2011; Torres-Freyermuth et al., 2010). However, models applicable for larger scale engineering and scientific applications often do not explicitly resolve the short waves. Instead, a so called phase-averaged approach is often used, in which a model that accounts for the nearshore transformation of short waves, providing the forcing on the wave group scale, is combined with a model based on the shallow-water equations, which accounts for the nearshore transformation of ig-waves (e.g. Roelvink et al., 2009). These models have been applied to simulate ig-waves underfield conditions and obtained reasonable agreement between model results and field data (e.g. List, 1992; Reniers et al., 2002, 2006, 2010; Van Dongeren et al., 2003, 2013). However, because they invariably use linear theory for the evolution of the short waves, they are less accurate under strongly nonlinear conditions. Moreover, they usually only include a one way coupling, in which wave energy can be transferred from the short waves to the ig-waves, but not vice-versa.

Models based on a Boussinesq type formulation (e.g. Madsen et al., 1991; Nwogu, 1993; Wei et al., 1995) or based on the non-hydrostatic approach (e.g. Ma et al., 2012; Stelling and Zijlema, 2003) are an alternative to the RANS and phase-averaged approach. These models aspire to resolve both the individual waves, including all the relevant processes (e.g. shoaling, refraction, diffraction, and nonlinearity) and the bulk dissipation associated with wave breaking, but not the detailed breaking process itself (e.g. wave overturning). Compared to RANS models this allows them to efficiently compute free surface flows by considering the free surface as a single-valued function. Boussinesq type models, introduced for variable depths by Peregrine (1967), have been applied extensively to the cross-shore evolution of short-wave motions, including wave breaking (e.g. Cienfuegos et al., 2010; Kennedy et al., 2000; Schäffer et al., 1993; Tissier et al., 2012; Tonelli and Petti, 2012) and to a lesser extent to ig-motions (e.g. Madsen and Sørensen, 1993; Madsen et al., 1997). Non-hydrostatic models were introduced more recently and have shown great potential for resolving the short-wave dynamics, including wave-breaking (e.g. Ma et al., 2012; Smit et al., 2013; Zijlema and Stelling, 2008) and the nonlinear wave-dynamics in a surf zone (Smit et al., 2014). Similar to RANS models, non-hydrostatic models are essentially implementations of the basic conservation equations for mass and momentum, that by using a reduced vertical resolution (two to three layers) have a similar computational effort and accuracy compared with Boussinesq models, whereas their implementation is less complex thereby improving robustness and maintenance. However, thus far, at coarse vertical resolutions non-hydrostatic models have not been verified for ig-waves.

In this study we show the capabilities of SWASH (Simulating WAVes till SHore, Zijlema et al., 2011), a non-hydrostatic type model, in reproducing the nearshore transformation of ig-waves. To include the generation of incident bound ig-waves, a wave-generating boundary condition – based on second order wave theory – has been implemented. Model results are compared with measurements of the flume experiment of Van Noorloos (2003) and Boers (1996).

The outline of this paper is as follows: §2 gives an overview of the governing equations of SWASH, including relevant details of its numerical implementation. In §3 we present the second-order boundary condition. The model validation for the Van Noorloos (2003) and Boers (1996) experiments is presented in §4 and §5, respectively. To conclude the paper, we discuss and summarise our main findings in §6 and §7.

2. Numerical model

2.1. Governing equations

The non-hydrostatic model SWASH (Zijlema et al., 2011) is a numerical implementation of the Reynolds-averaged Navier–Stokes

equations for an incompressible fluid with a constant density and a free surface. In a two-dimensional framework that is bounded by the free surface $z = \zeta(x,t)$ and the bottom $z = -d(x)$, where t is time and x and z are Cartesian co-ordinates ($z = 0$ is located at the still water level), the governing equations read

$$\frac{\partial u}{\partial t} + \frac{\partial uu}{\partial x} + \frac{\partial wu}{\partial z} = -\frac{1}{\rho} \frac{\partial (p_h + p_{nh})}{\partial x} + \frac{\partial}{\partial x} \left(\nu^h \frac{\partial u}{\partial x} \right) + \frac{\partial}{\partial z} \left(\nu^v \frac{\partial u}{\partial z} \right), \quad (1)$$

$$\frac{\partial w}{\partial t} + \frac{\partial uw}{\partial x} + \frac{\partial ww}{\partial z} = -\frac{1}{\rho} \frac{\partial (p_h + p_{nh})}{\partial z} + \frac{\partial}{\partial x} \left(\nu^h \frac{\partial w}{\partial x} \right) + \frac{\partial}{\partial z} \left(\nu^v \frac{\partial w}{\partial z} \right) - g, \quad (2)$$

$$\frac{\partial u}{\partial x} + \frac{\partial w}{\partial z} = 0, \quad (3)$$

where $u(x,z,t)$ is the horizontal velocity, $w(x,z,t)$ is the vertical velocity, ν^h and ν^v are the horizontal and vertical kinematic eddy viscosities, respectively, g is the gravitational acceleration, and p_h and p_{nh} are the hydrostatic and non-hydrostatic pressures, respectively. The hydrostatic pressure is expressed in terms of the free surface as $p_h = \rho g(\zeta - z)$ such that $\partial_z p_h = -\rho g$ (where ∂_z is short for $\partial/\partial z$) and $\partial_x p_h = \rho g \partial_x \zeta$. An expression for the free surface is obtained by considering the (global) mass balance for the entire water column

$$\frac{\partial \zeta}{\partial t} + \frac{\partial}{\partial x} \int_{-d}^{\zeta} u dz = 0. \quad (4)$$

For waves propagating over intermediate distances (say $O(10)$ wave lengths), in the absence of strongly sheared currents, turbulence has only marginal effects on the wave motion and can – to a good approximation – be neglected. Furthermore, the above equations (excluding the turbulence terms) can be directly applied to estimate the overall characteristics of a quasi-steady breaking bore in the surf zone, without the need to resolve complex phenomena such as the wave generated turbulence. Therefore, turbulent stresses can be neglected in this study. However, to increase numerical stability and to allow the influence of bottom friction to extend over the vertical, we introduce some vertical mixing by means of the vertical exchange of momentum due to turbulent stresses with a constant $\nu^v (= 10^{-4} \text{ m}^2/\text{s})$.

Kinematic and dynamic boundary conditions are prescribed at the free surface and bottom, given by

$$\begin{aligned} w(x, z = \zeta, t) &= \frac{\partial \zeta}{\partial t} + u \frac{\partial \zeta}{\partial x}, \\ w(x, z = -d, t) &= -u \frac{\partial d}{\partial x}. \end{aligned} \quad (5)$$

These boundary conditions ensure that no particle leaves the surface and no particle penetrates the fixed bottom. At the free surface the dynamic boundary condition prescribes a constant pressure ($p_{nh} = p_h = 0$) and no surface stresses. At the bottom boundary a bottom stress term is added to the horizontal momentum Eq. (1) as bottom friction is important for the low-frequency motions, for which it is one of the mechanisms of energy dissipation. The bottom stress is based on a quadratic friction law $\tau_b = c_f \frac{u|u|}{h}$, where $h = d + \zeta$ is the total water depth, c_f is a dimensionless friction coefficient and U is the depth-averaged velocity. Feddersen et al. (2003) found that the friction coefficient is enhanced in the surf zone due to the presence of breaking waves. In this study we compute the friction coefficient based on the Manning–Strickler formulation, which reads $c_f = 0.015(d_r/h)^{1/3}$ where d_r is an (apparent) roughness value. Although this formulation was derived for slowly varying open-channel flows and not for rapidly varying flows such as in the surf zone, it gives increasing values of c_f for decreasing depths which

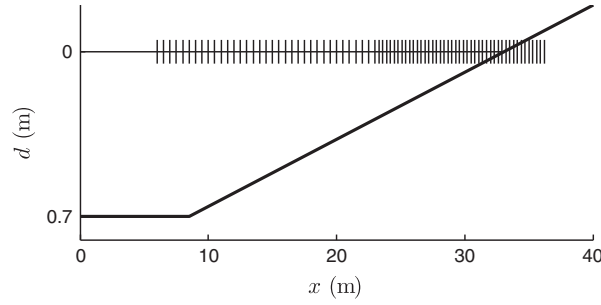


Fig. 1. Van Noorloos (2003) experimental set-up. The still water level is located at $z = 0$ m and the vertical lines indicate the gauge locations.

makes it a suitable proxy to mimic the wave breaking enhanced roughness. The disadvantage of this formulation is that the roughness value cannot easily be estimated a priori and instead – as will be done in this study – needs to be calibrated.

Waves are generated at the wavemaker boundary (situated at $x = 0$ m) by prescribing the horizontal velocity $u(x = 0, z, t)$ obtained from second-order wave theory, which will be described in detail in §3. At the shore we employ a moving shoreline boundary condition to accurately simulate wave run-up and flooding and drying (Stelling and Duinmeijer, 2003).

2.2. Numerical implementation

The numerical implementation is based on an explicit, second-order accurate (in space and time) finite difference method that conserves both global mass and momentum at the numerical level. Local mass conservation, corresponding to a divergence-free velocity field, is obtained by means of a pressure correction technique. A structured grid is employed to discretise the physical domain. In x -direction the grid has a constant width whereas in vertical direction the physical domain is divided into a fixed number of layers (K) between the bottom and the free surface, which results in a (spatially varying) layer thickness of $\Delta z = h/K$. A more detailed overview of the numerical implementation is given in Zijlema et al. (2011) and references therein. With the numerical implementation used in the SWASH model, good wave dispersive properties are found even for low vertical resolutions (Smit et al., 2014; Zijlema et al., 2011). For instance, with two vertical layers (as used in this study) the relative error in the phase velocity (compared with the linear dispersion relation) is approximately 1% up to $kd \approx 8$, where k is the wave number. This allows SWASH to account for the relevant physics outside the surf zone (refraction, shoaling, diffraction, non-linear interactions) with a relative coarse vertical resolution.

In the surf zone, SWASH intrinsically accounts for the energy dissipation of a breaking wave. Once the wave height over depth ratio becomes $\mathcal{O}(1)$, a discontinuity develops as a wave steepens up and develops a vertical face. In such a situation, as the model conserves momentum over the discontinuity using shock-capturing dynamics, energy is dissipated at a rate analogous with that of a bore (Lamb, 1932). However, compared with the resolution outside the surf zone, this requires a high vertical resolution ($\mathcal{O}(10)$ vertical layers) to reproduce the observed locations of incipient wave breaking, whereas at low vertical resolutions wave breaking is delayed (Smit et al., 2013). At present, such high vertical resolutions are not feasible for relatively large horizontal domains (e.g. 10×10 wavelengths). To capture wave breaking with only a few vertical layers, Smit et al. (2013) proposed an approach with which the non-hydrostatic pressure is neglected in the vicinity of a breaking wave. This (locally) reduces the governing equations to the nonlinear shallow water equations and ensures that a wave develops a vertical face. This approach is initiated once the rate of change of the free surface exceeds a certain threshold ($\partial_t \zeta / \sqrt{gh} > \alpha$, where α is the threshold).

Once initiated, α is reduced to β (with $\beta < \alpha$) in neighbouring points to allow breaker persistence. In this study we use the values for $\alpha (= 0.6)$ and $\beta (= 0.3)$ found by Smit et al. (2013) for two vertical layers, for which good results were obtained for various flume and basin experiments.

3. A second-order boundary condition to generate incident bound ig-waves

At the model wavemaker the normal horizontal velocity based on second-order wave theory is prescribed to generate incident waves. In this study we only incorporate the difference interactions (i.e. bound ig-waves) and we exclude the sum interactions (i.e. bound super harmonics) for efficiency reasons.¹ The incident (target) horizontal velocity u_t at the boundary is given by

$$u_t(x = 0, z, t) = \sum_{n=1}^N \hat{u}_n(z) \cos(2\pi f_n t + \phi_n) + \sum_{n=1}^N \sum_{m=n+1}^N \hat{u}_{nm} \cos(2\pi f_{nm} t + \phi_{nm}), \quad (6)$$

where N is the number of free wave components. The first term on the right-hand-side of (6) represents the linear free wave contribution, where f_n is the frequency, ϕ_n is the phase and $\hat{u}_n(z)$ is the vertically varying velocity amplitude of the n th wave component which is related to the short-wave amplitude a_n by linear wave theory (e.g. Holthuijsen, 2007). The second summation is the second-order correction which represents the contribution of the incident bound ig-waves, where $f_{nm} (= f_m - f_n)$ is the frequency, $\phi_{nm} = (\phi_n - \phi_m + \pi)$ is the phase and \hat{u}_{nm} is the vertically varying velocity amplitude of the bound ig-wave component forced by the difference interaction between the n th and m th free wave component. In coastal waters, ig-waves are essentially shallow-water waves for which the vertical variation of \hat{u}_{nm} is negligible. Therefore, we approximate \hat{u}_{nm} with a vertically constant velocity amplitude, which is computed based on the free wave components following Hasselmann (1962), see Appendix A.

To prevent re-reflections at the wavemaker a weakly reflective boundary condition is adopted in which the total velocity signal $u(x = 0, z, t)$ is a superposition of the incident, or target, velocity signal (u_t) and a velocity signal of the reflected waves (u_r), i.e. $u = u_t + u_r$. To estimate the velocity of the reflected wave signal we assume that the reflected waves are shallow water waves, which implies that all short waves have dissipated inside the domain. This allows us to

¹ The exclusion of the sum interactions at the model boundary does not imply that the bound super harmonics are absent, instead, in addition to the bound higher harmonics, spurious free waves are generated at the sum frequencies (see also Appendix B). Because the energy contained in such spurious modes is comparable to the bound energy (which is small compared with the energy in the primary waves), the influence of the additional spurious energy is small, and will not adversely affect the nearshore transformation of the high frequency band.

Table 1

Wave parameters at the boundary for the bichromatic wave experiments. Listed are the primary wave frequencies f and amplitudes a ; bound wave frequency f_b and the maximum normalised water depth kd .

	f_1 (Hz)	f_2 (Hz)	f_b (Hz)	a_1 (m)	a_2 (m)	kd
A1	0.67	0.48	0.19	0.06	0.012	2.00
A2	0.65	0.50	0.15	0.06	0.012	1.94
A3	0.64	0.51	0.13	0.06	0.012	1.90
A4	0.62	0.53	0.09	0.06	0.012	1.81
B1	0.65	0.50	0.15	0.06	0.018	1.95
B2	0.65	0.50	0.15	0.06	0.024	1.95
B3	0.65	0.50	0.15	0.06	0.030	1.95
B4	0.65	0.50	0.15	0.06	0.036	1.95

compute the depth averaged horizontal velocity u_r based on the surface elevation of the outgoing waves, which is detected as the difference between the target surface elevation ζ_t and the instantaneous surface elevation ζ computed by SWASH. The u_r follows from mass conservation in combination with the assumption that outgoing waves are progressive and of constant form,

$$u_r = \frac{c}{d}(\zeta - \zeta_t), \quad (7)$$

where c is the phase velocity, which is taken as the shallow water phase velocity $c = \sqrt{gd}$.

We have verified the accuracy of the second-order weakly-reflective boundary condition in reproducing the classical finite depth solution of Longuet-Higgins and Stewart (1960) for bound ig-waves, induced by a bichromatic wave group which propagates over a flat bottom. With two or more vertical layers the solution of Longuet-Higgins and Stewart (1960) is reproduced well if the short waves that form the wave group are in shallow to intermediate water depths ($kd < 2.5$) (Appendix B).

4. Infragravity waves induced by bichromatic waves over a plane slope

Van Noorloos (2003) considered the evolution of bichromatic wave groups as they propagate in a 40 m long flume over a 1 / 35 plane slope

(see Fig. 1). An interesting feature of these experiments is that they confirmed that dissipation due to ig-wave breaking can be one of the primary mechanisms of ig-wave dissipation (Van Dongeren et al., 2007). In these experiments the flume was equipped with a piston-type wave board, which included second-order wave control and reflection compensation. Van Noorloos (2003) considered eight bichromatic wave conditions which varied in wave magnitude (B1–4, see Table 1) and in bound ig-wave frequency (f_b) (A1–4, see Table 1), where the latter in particular is associated with varying ig-wave conditions. In these experiments ig-wave conditions ranged between strong ig-wave dissipation (due to ig-wave breaking) and small ig-wave reflections near the shoreline (experiment A1) to strong ig-wave reflections (experiment A4) (Van Dongeren et al., 2007). Measurements of the free surface were taken at 80 locations, with a spacing varying from 0.5 m to 0.3 m, for a duration of 10 min.

SWASH is employed with two vertical layers to accurately capture the wave dispersion, and the bound ig-wave response (Appendix B), for the range of kd values encountered (see Table 1). The grid resolution is set at $\Delta x = 0.01$ m, which corresponds to at least 20 points per wave length for the super harmonic wave components, and the time step is set at $\Delta t = 0.002$ s. The incoming boundary is located at the first wave gauge ($x = 6$ m) and we employ a second-order accurate weakly-reflective boundary to generate incident waves (§3), according to the target wave conditions (Table 1). The roughness coefficient $d_r (= 0.0075$ m) was calibrated for the experiment which featured the

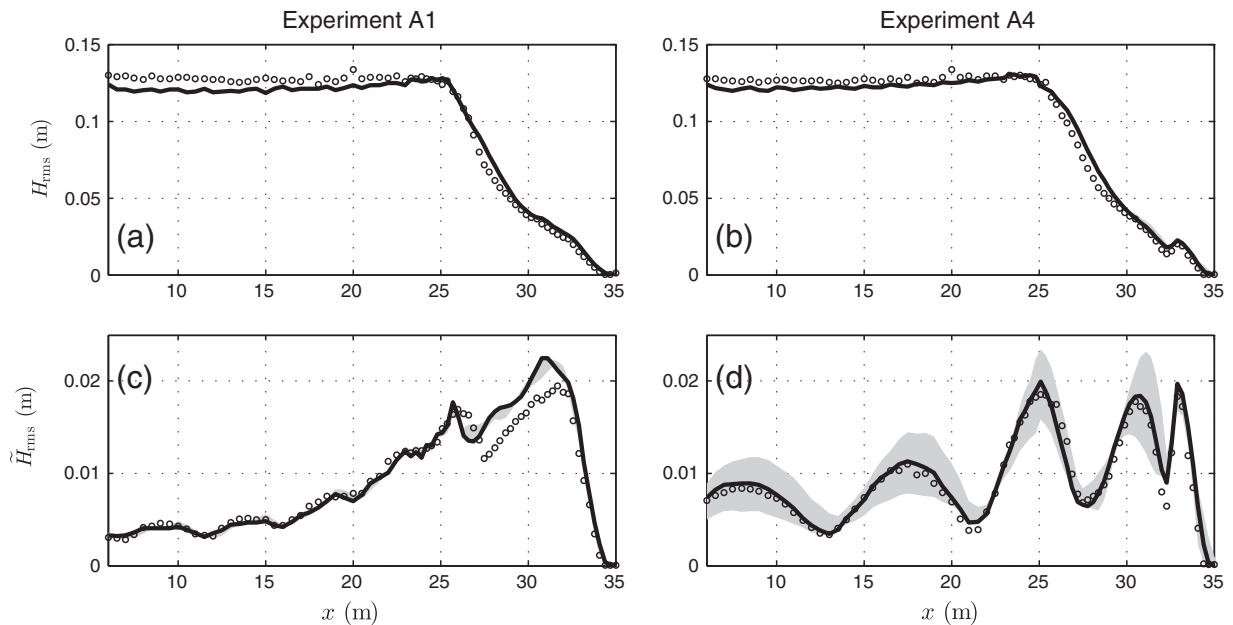


Fig. 2. Cross-shore variation of the H_{rms} (upper panels) and the \tilde{H}_{rms} (lower panels) for experiment A1 (left panels) and A4 (right panels). Comparison between measured (circles) and computed values (lines). The grey region gives the range in wave heights found when varying the roughness coefficient.

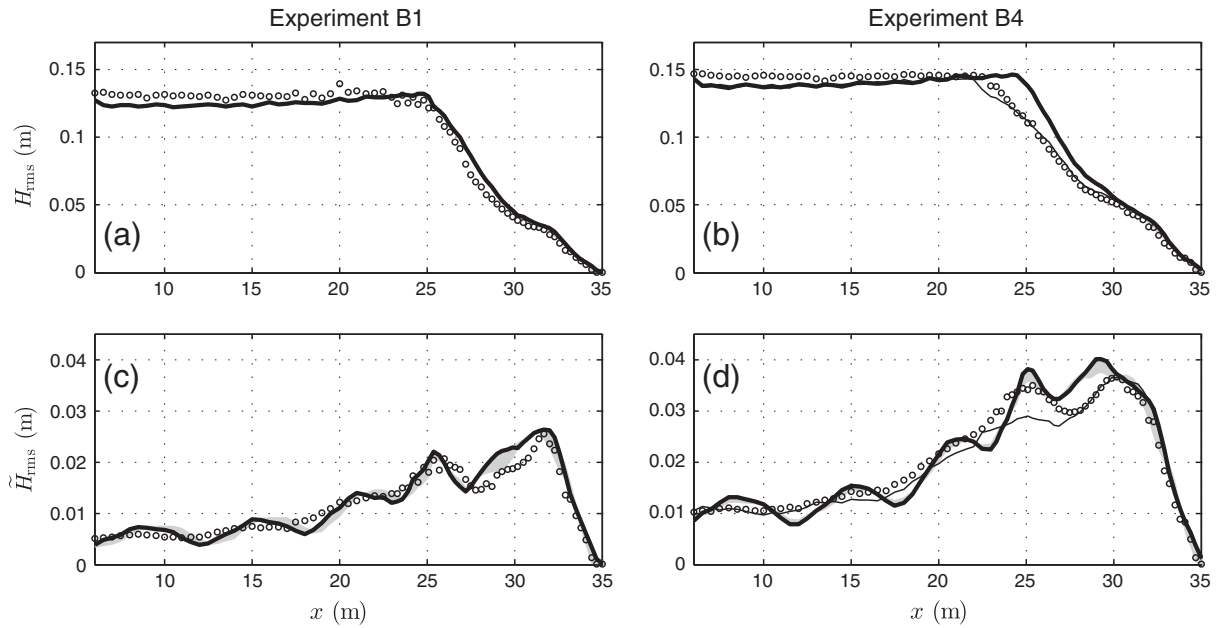


Fig. 3. Cross-shore variation of the H_{rms} (upper panels) and the \tilde{H}_{rms} (lower panels) for experiment B1 (left panels) and B4 (right panels). Comparison between measured (circles) and computed values (lines). The grey region gives the range in wave heights found when varying the roughness coefficient. The thin black line in panel b and d is calculated with $\alpha = 0.5$.

strongest ig-wave reflections (A4), where we expect a significant influence of the bottom friction on the ig-wave dynamics. In the following, the analysis is based on the measured and computed free surface elevation records after steady state conditions were observed, five minutes after the start of the simulation (Van Dongeren et al., 2007).

4.1. Results

First we compare the predicted and measured cross-shore transformation of the bulk wave parameters for experiments A1, A4, B1 and B4. Here, we compare measured and predicted root-mean-

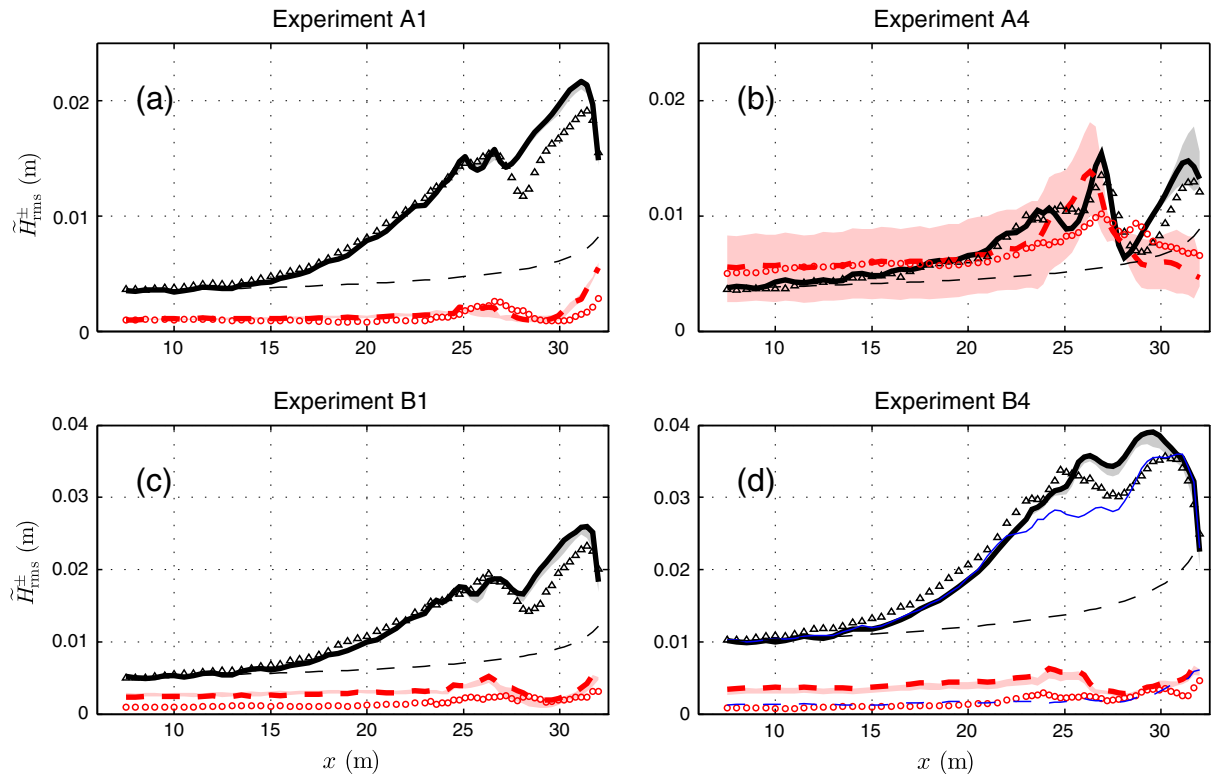


Fig. 4. Cross-shore variation of incoming \tilde{H}_{rms}^+ and outgoing ig-wave heights \tilde{H}_{rms}^- for experiment A1 (panel a), A4 (panel b), B1 (panel c) and B4 (panel d). Comparison between measured (incoming component: black triangles, outgoing component: red circles) and predicted values (incoming component: solid black line, outgoing component: dashed red line). The black dashed curve indicates Green's law for energy conservative shoaling ($H \propto d^{-1/4}$), initiated with the predicted incident incoming ig-wave height. The shaded regions give the range in wave heights found when varying the roughness coefficient (incoming component: grey, outgoing component: light red). The thin blue lines panel d are calculated with $\alpha = 0.5$.

square wave heights H_{rms} , which are computed from the variance of linearly detrended surface elevation signals, $H_{rms} = \sqrt{8\langle \tilde{\zeta}^2 \rangle}$, where $\langle \dots \rangle$ indicates time averaging. To analyse the nearshore transformation of ig-waves, the surface elevation signals have to be filtered. The occurrence of ig-wave breaking in some of the experiments indicates that strong nonlinear effects play a dominant role in the evolution of the ig-waves close to the shoreline. Near the shore not only the high-frequency waves, but also the ig-waves transition into sawtooth like-shapes, which in the spectral domain is associated with the generation of significant energy at the higher harmonics of the ig-wave frequencies. For this reason, we filter the surface elevation signal using a band pass filter that includes the difference frequency ($\Delta f = f_1 - f_2$) and integer multiples thereof ($m\Delta f$ for $m = 2 \dots f_{nyq}/\Delta f$, where f_{nyq} is the Nyquist frequency). This method is applicable as the variance at the $m\Delta f$ frequencies is attributed to ig-wave self-interactions and not to (interactions of) higher-frequency components (Van Dongeren et al., 2007). In the remainder of this section we use a tilde accent ($\tilde{}$) to denote variables computed from the filtered signal.

The variation of the measured wave height H_{rms} is similar in experiment A1, A4, B1 and B4 (see Figs. 2a–b and 3a–b). In all four cases H_{rms} remains nearly constant on the flat ($x < 8.5$ m) and at the

start of the slope, and reduces rapidly in the surf zone once breaking is initiated ($x \approx 25$ m). For all cases predicted and measured H_{rms} are in agreement, except for B4 where the predicted position of incipient short-wave breaking is located further shoreward than the observed location (Fig. 3b). For B4, the predicted location of wave breaking can be improved with a slightly smaller breaking threshold ($\alpha = 0.5$), see Fig. 3b.

The aforementioned difference in ig-wave behaviour for the different incident wave conditions, i.e. reflective or dissipative, can be seen by comparing the cross-shore variation of the measured ig-wave height \tilde{H}_{rms} for experiment A1 and A4 (see Fig. 2c–d). In A1, \tilde{H}_{rms} increases in shoreward direction with a small oscillation for $x < 25$ m. As the short waves start to break ($x \approx 25$ m) \tilde{H}_{rms} decreases, up to $x \approx 27$ m where it increases again. For $x > 31$ m, \tilde{H}_{rms} decreases significantly. In experiment A4 the cross-shore variation of \tilde{H}_{rms} has a nodal structure with an increasing magnitude towards the shore. The nodal structure is associated with the occurrence of a standing ig-wave. For experiment B1 and B4 the nearshore transformation of the \tilde{H}_{rms} is similar to A1 (see Fig. 3c–d). For all cases predicted and measured \tilde{H}_{rms} are in agreement, except for a discrepancy for $26 \text{ m} < x < 32 \text{ m}$ in A1 and B1, where \tilde{H}_{rms} is over estimated due to an over prediction of the incoming ig-wave height, and in B1 and (especially) B4, where the predicted oscillation of \tilde{H}_{rms} for $x < 25$ m is

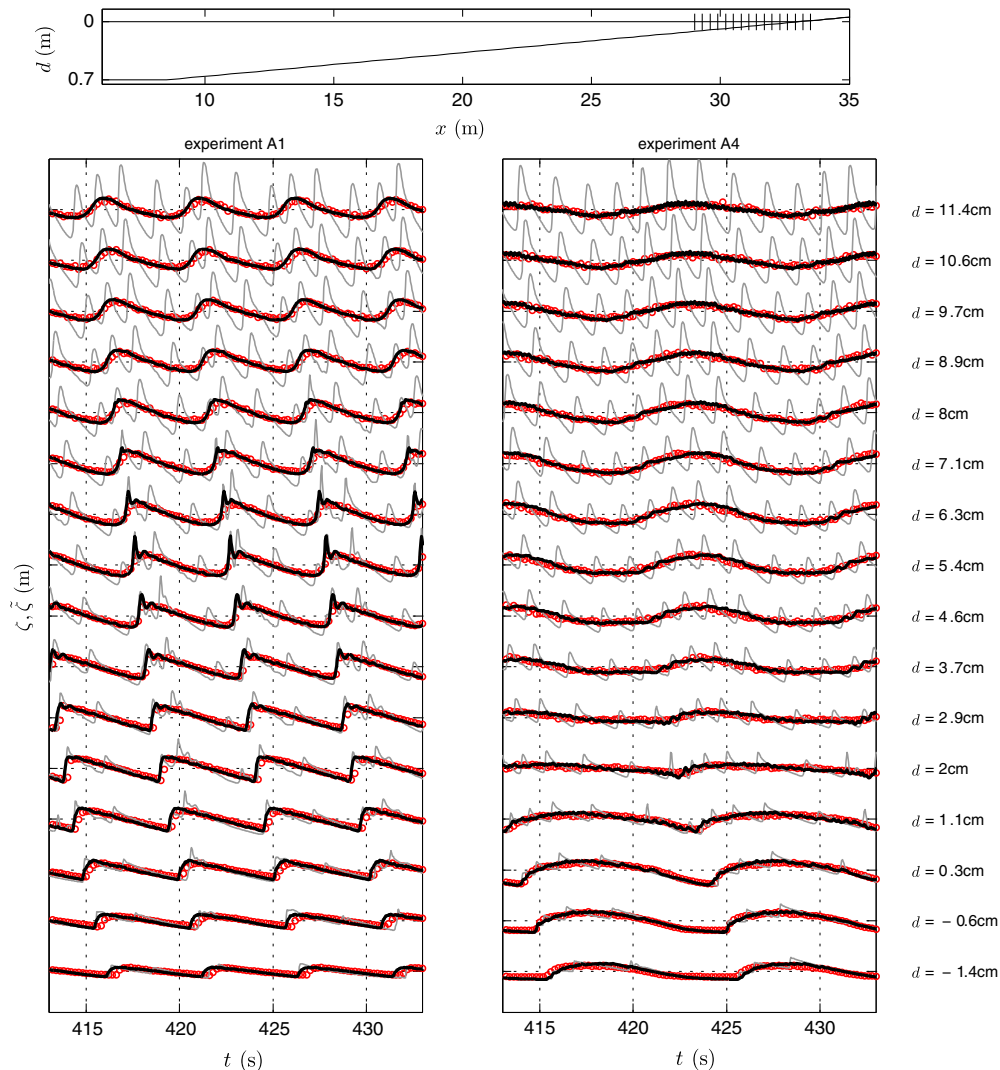


Fig. 5. Time series of the infragravity wave signal $\tilde{\zeta}$ at several gauge locations close to the shoreline for experiment A1 (left panel) and A4 (right panel). Measurements (markers); SWASH results (solid line). The grey line is the computed surface elevation. The top panel shows the bathymetry and gauge locations.

more pronounced than in the measurements due to an over prediction of the outgoing ig-wave height.

Incoming ig-waves are generally bound to the wave group, such that their behaviour no longer corresponds to that of a free wave. In contrast reflected ig-waves are free waves as the high-frequency motion is almost entirely destroyed in the surf zone. The different character of the incoming and outgoing low-frequency motion makes it interesting to consider them separately. To distinguish between these two components, we decompose the ig-wave signal with the decomposition method of Battjes et al. (2004), as used by Van Dongeren et al. (2007). In A1, B1 and B4 measured outgoing ig-wave heights \tilde{H}_{rms}^- are small compared to measured incoming ig-wave heights \tilde{H}_{rms}^+ (Fig. 4a,c-d), which indicates that the shoreline reflection and the contribution of breakpoint induced ig-waves are small. In the measurements, incoming ig-waves grow towards the shore with a growth rate which exceeds Green's law for energy conservative shoaling ($H \propto d^{-1/4}$). For $x > 25$ m measured \tilde{H}_{rms}^+ decreases, up to $x \approx 27$ m where it increases again. Close to the shore \tilde{H}_{rms}^+ starts to decrease significantly, which is associated with ig-wave breaking (Van Dongeren et al., 2007). The cross-shore variation of \tilde{H}_{rms}^+ and \tilde{H}_{rms}^- are very similar which further illustrates the dominance of incoming ig-waves. For A4 the growth of \tilde{H}_{rms}^+ is small compared to the other three experiments, whereas the magnitude of \tilde{H}_{rms}^- is larger (Fig. 4b). Predicted and measured incoming and outgoing wave heights are in agreement throughout the domain for all experiments, apart from an over prediction of \tilde{H}_{rms}^+ inside the surf zone ($x > 26$ m) in A1 and B1, a local over prediction of \tilde{H}_{rms}^- at $x \approx 26$ m in A4, and a significant over prediction of \tilde{H}_{rms}^- throughout the domain in B1 and B4. Discrepancies between predicted and measured

ig-wave heights are most significant for experiment B4, for which we previously observed that short-wave breaking is delayed in SWASH (Fig. 3b). Not only does reducing the breaking threshold ($\alpha = 0.5$) improve predicted H_{rms} (Fig. 3b), it also improves predictions of \tilde{H}_{rms} , \tilde{H}_{rms}^+ and \tilde{H}_{rms}^- (Figs. 3d and 4d), which indicates that the over prediction of \tilde{H}_{rms}^- is related to the delayed short-wave breaking.

To investigate the influence of the roughness coefficient on the model results, additional simulations were executed with a roughness coefficient ranging $d_r = 0.001 - 0.02$ m. The shaded regions in Figs. 2–4 are the regions between the maximum and minimum of H_{rms} , \tilde{H}_{rms} and \tilde{H}_{rms}^+ for the simulations with the various roughness coefficients. The low sensitivity of H_{rms} to variations in d_r implies that bottom friction – as anticipated – has only a marginal influence on the nearshore transformation of short waves (Figs. 2–3). Similarly, if ig-waves are breaking, ig-wave energy losses are dominated by ig-wave breaking and the influence of variations in d_r is small (Fig. 4a, c-d). Only for a strong reflective condition (A4), variations in d_r do significantly influence ig-wave heights. Nevertheless, the nodal pattern is correctly reproduced for all values of d_r (Fig. 2d). In all experiments, but most significantly for A4, bottom friction predominantly influences outgoing ig-wave heights (Fig. 4b), which indicates that friction is primarily of significance in the inner surf zone ($x > 30$ m).

IG-wave breaking can be observed when inspecting the time signals of the ig-wave surface elevation at several gauge locations near the shoreline, which is similar to an analysis in Van Dongeren et al. (2007). In experiment A1, as the ig-waves enter progressively shallower water, the ig-wave front develops an almost vertical face and subsequently rapidly decreases in height (Fig. 5). This pattern is very

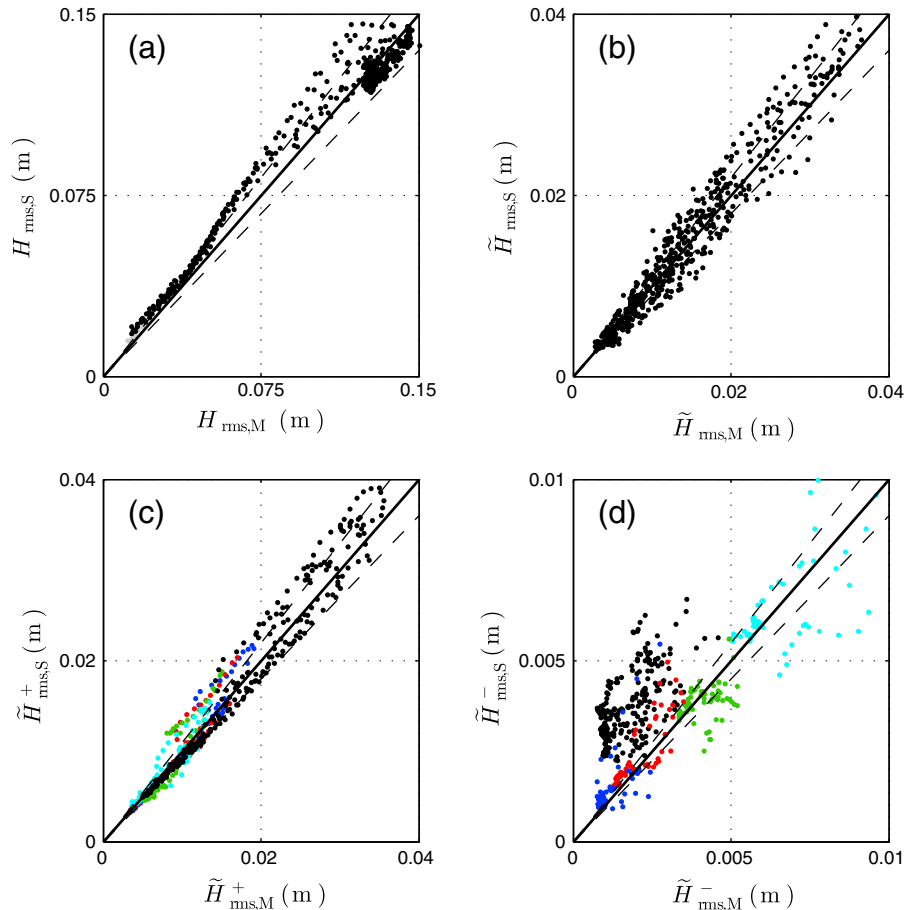


Fig. 6. Predicted (subscript S) versus measured (subscript M) wave heights for the total wave height H_{rms} (a), ig-wave height \tilde{H}_{rms} (b), incoming ig-wave height \tilde{H}_{rms}^+ (c) and outgoing ig-wave height \tilde{H}_{rms}^- (d). In panel c and d, a distinction is made between the various ig-wave conditions, ranging from dissipative (A1) to reflective (A4), using the following colours: A1 (blue); A2 (red); A3 (green); A4 (cyan) and B1-4 (black). The solid line indicates one to one correspondence and the dashed lines are the 10% error bands.

Table 2
Skill factors for the van Noorloos experiments.

	H_{rms}	\tilde{H}_{rms}	\tilde{H}_{rms}^+	\tilde{H}_{rms}^-
A1-4	0.95	0.85	0.85	0.70
B1-4	0.92	0.87	0.89	-0.07
Overall	0.94	0.86	0.87	0.32

similar to that of a breaking wave and suggests that ig-waves are breaking. A similar analysis for experiment A4 shows no sign of ig-wave breaking in both measured and computed surface elevation signals (Fig. 5). For both cases, computed wave signals are in agreement with the observations.

Finally, we consider the model performance for all bichromatic wave experiments. To quantify the accuracy of the model we compute the model skill as (e.g. Reniers et al., 2006),

$$\text{Skill} = 1 - \frac{\sqrt{\frac{1}{N} \sum_{n=1}^N (X_p - X_o)^2}}{\sqrt{\frac{1}{N} \sum_{n=1}^N (X_o)^2}}, \quad (8)$$

where N is the total number of observations and X is the considered quantity with subscript p and subscript o denoting predicted and observed values. Predicted H_{rms} agree well with the observations (Fig. 6), as indicated by the overall skill factor of 0.94 (Table 2). Similarly, predicted and observed \tilde{H}_{rms} agree for all experiments, although the scatter is larger and the overall skill is lower compared to the results for H_{rms} . Predicted and measured \tilde{H}_{rms}^+ agree well and the skill is similar to that of \tilde{H}_{rms} . In contrast, errors in the predicted \tilde{H}_{rms}^- are large as indicated by the low overall skill. The errors in the predicted \tilde{H}_{rms}^- are largest for the results of experiment B1-4, for which the skill factor is negative which indicates that errors in predicted \tilde{H}_{rms}^- are larger than measured \tilde{H}_{rms}^- . For these dissipative ig-wave conditions, outgoing ig-wave energies are very small and minor errors in the modelled dissipation can result in large errors in outgoing ig-wave energies. To illustrate this we consider the relative difference between the incoming and outgoing infragravity energy flux D . If we assume that the group velocity of the incoming and outgoing ig-waves are approximately equal in magnitude, we can define D as

$$D = 100 \frac{|\tilde{E}^+ - \tilde{E}^-|}{\tilde{E}^+}, \quad (9)$$

where \tilde{E}^\pm is the energy of an incoming (+) or outgoing (-) ig-wave component at the outer edge of the surf zone ($x = 25$ m). This shows that in experiment A1, B1-4 ig-wave energy losses are large and that errors in predicted D are small ($\approx 3\%$, see Table 3), which indicates that SWASH captures the bulk energy dissipation of a breaking ig-wave. Although the errors in the bulk dissipation are small for experiment B1-4, the model skill for the outgoing ig-wave heights is low, which indicates that small errors in the predicted bulk dissipation of a breaking ig-wave can result in large errors in the predicted outgoing ig-wave heights.

5. Infragravity waves induced by random waves over a barred beach

The second flume experiment we consider in this study was performed by Boers (1996), who considered irregular waves

Table 3
Relative ig-wave energy losses D (%) in the surf zone for the van Noorloos experiments.

	A1	A2	A3	A4	B1	B2	B3	B4
Measurements	98.5	95.9	80.2	37.2	98.4	98.5	99.3	99.7
SWASH	98.3	92.8	76.8	45.5	95.2	95.1	96.7	96.6

propagating over a barred beach (see Fig. 7) in the same flume as Van Noorloos (2003). A variety of incident wave conditions were simulated with this set-up of which the lowest steepness wave condition (1C) has been analysed extensively in other studies (e.g. Battjes et al., 2004; Janssen et al., 2003). Here we shall also analyse this case, in which the shoaling of ig-waves was most distinct, as it is the most relevant wave condition for studying the ig-wave dynamics. In experiment 1C waves were generated at the wavemaker based on a target JONSWAP spectrum with a significant wave height of 0.103 m and a peak period of 3.33 s. Measurement of the free surface were taken at 70 locations, with intervals varying from 1 m to 0.18 m, for a duration of 28 min.

SWASH is employed with two vertical layers to capture the bound ig-wave response (Appendix B) and the propagation of short waves with frequencies up to three times the peak frequency f_p (with $kd = 2.5$). The grid resolution is set at $\Delta x = 0.02$ m, which corresponds to at least 20 points per wave length for waves up to $3f_p$, and the time step is set at $\Delta t = 0.002$ s. The incoming boundary is located at the first wave gauge and we employ a second-order accurate weakly reflective boundary condition (§3) based on the free wave components. The target free wave components with which the wavemaker in the flume is forced are not available and no velocities were measured near the wavemaker. Therefore, the incident free wave components can only be obtained based on measurements of the free surface at the first wave gauge. We estimate these components using the Fourier transform and a high-pass filter of $f > f_p/2$ to remove most bound ig-wave components, since their contribution is accounted for by including the theoretical second-order response. The roughness coefficient is set at the same value as in the previous laboratory case ($d_r = 0.0075$ m). The model and measured signals are analysed excluding a spin-up time of 60 s ($> 4L_s/c_g$, where L_s is the length of the flume and c_g is the group velocity according to the peak frequency at the wavemaker).

5.1. Results

First we compare measured and predicted significant wave heights $H_{m0} (= 4\sqrt{m_0})$ and periods $T_{m01} (= \sqrt{m_0/m_1})$ of short- and ig-waves, where the moments $m_n (= \int f^n E(f) df)$ are computed from the variance density spectra $E(f)$ of the free surface elevation. The variance density spectra are computed with smoothing in the frequency domain and have 30 degrees of freedom. To distinct between short and ig-waves, we compute their bulk parameters from the band-passed filtered variance density with a band pass of $0.5f_p < f \leq 4f_p$ and $0.1f_p < f \leq 0.5f_p$, respectively. We take the peak frequency as the peak frequency at the wavemaker ($f_p = 0.3$ Hz). In the remainder of this section parameters calculated from the high-frequency band are denoted with a prime accent ('), and parameters computed from the low-frequency band with a tilde accent (~).

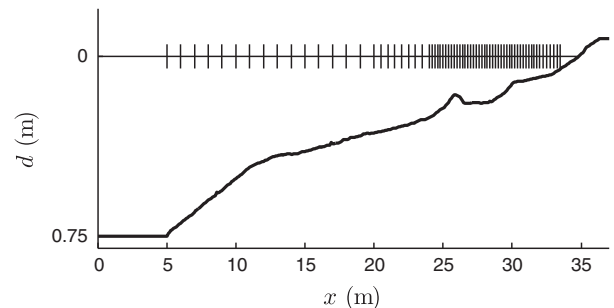


Fig. 7. Boers (1996) experimental set-up. The still water level is located at $z = 0$ m and the vertical lines indicate the gauge locations.

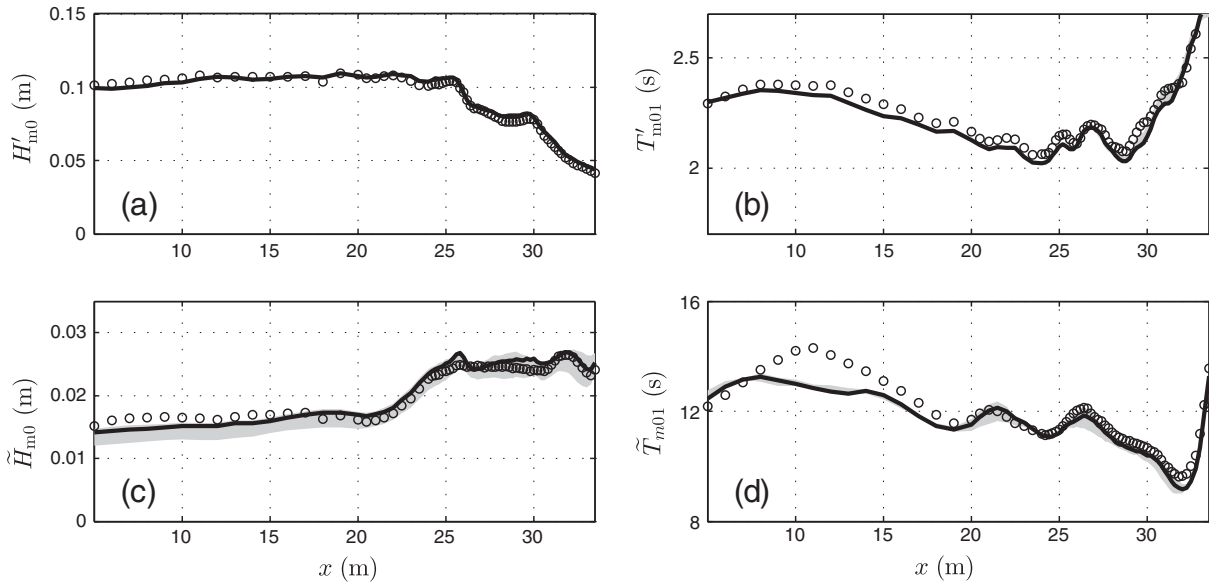


Fig. 8. Cross-shore variation of the significant wave heights H_{m0} (panel a and c) and mean wave periods T_{m01} (panel b and d) of short waves (panel a and b) and ig-waves (panel c and d). Comparison between measured (markers) and predicted values (line). The grey region gives the range in wave heights found when varying the roughness coefficient.

The predicted bulk wave parameters (significant wave height and mean wave period) of both short and ig-waves are in agreement with the measurements throughout the domain (Fig. 8), despite an under prediction of \tilde{T}_{m01} for $8 \text{ m} < x < 20 \text{ m}$.

To quantify the magnitude of incoming and outgoing ig-wave components, we employ the improved signal decomposition method (Van Dongeren et al., 2003) of Battjes et al. (2004) with nine sensors for lower frequencies ($f \leq 0.11 \text{ Hz}$) and five for the remaining higher

frequencies ($f \leq f_p/2$). This is the same number of sensors as Battjes et al. (2004) used in their analysis of the same data set. The measured \tilde{H}_{m0}^+ increases in shoreward direction with a rate which exceeds Green's law for energy conservative shoaling (Fig. 9a). As the short waves break ($x > 25 \text{ m}$), the growth rate of incoming ig-waves reduces but remains positive throughout most of the surf zone ($x > 25 \text{ m}$). Outgoing ig-waves decrease in height as they propagate in off-shore direction, in accordance with Green's law. Throughout the domain measured

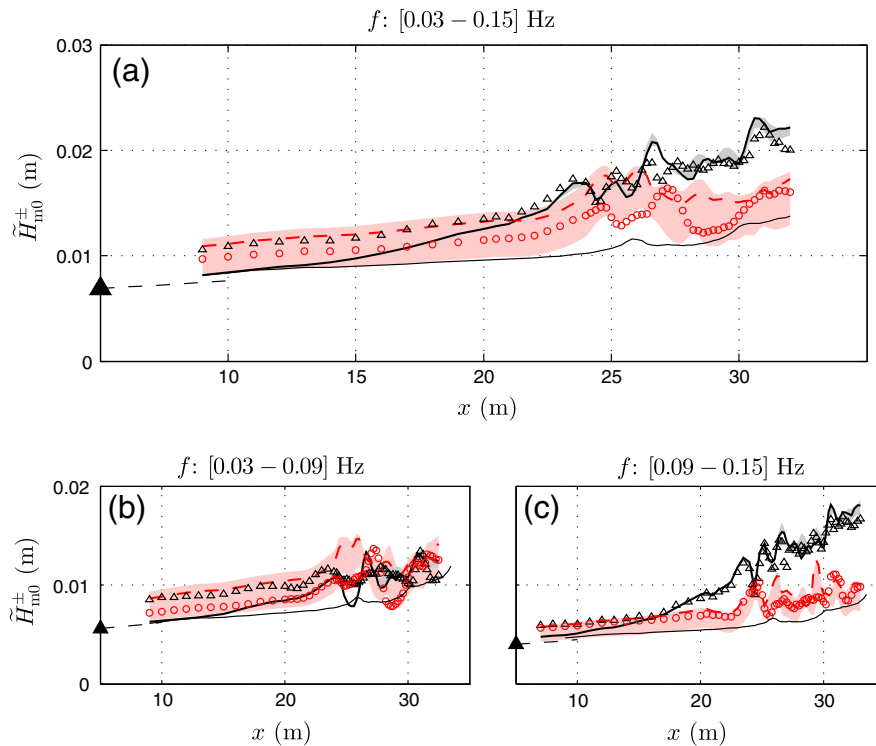


Fig. 9. Cross-shore variation of incoming \tilde{H}_{m0}^+ and outgoing ig-wave heights \tilde{H}_{m0}^- , computed by integration over different frequency bands. Comparison between measured (incoming component: black triangles, outgoing component: red circles) and predicted values (incoming component: black line, outgoing component: dashed red line). The shaded regions indicate the maximal and minimal wave heights encountered in the simulations with a variation in the roughness coefficient (incoming component: grey, outgoing component: light red). The shaded triangle is the target bound ig-wave height and the thin black curves indicates Green's law for energy conservative shoaling ($H \propto d^{-1/4}$), initiated with either the predicted incoming ig-wave height at $x = 9 \text{ m}$ (full line), or the target bound ig-wave height (dashed line).

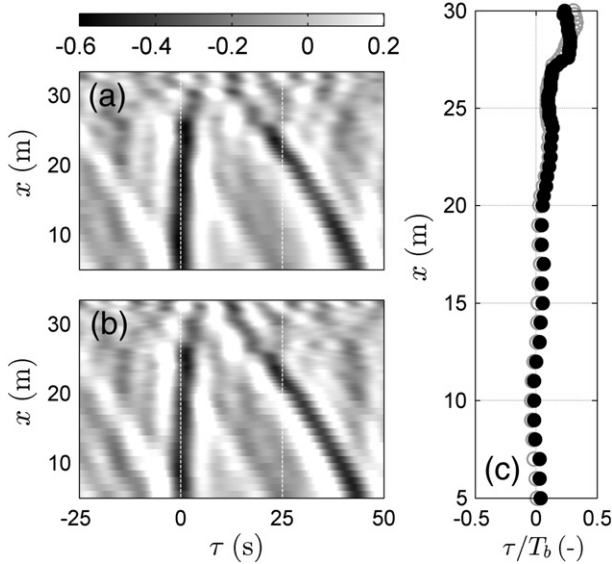


Fig. 10. Cross-correlation between the squared wave envelope and the ig-wave surface elevation signal for the measurements (panel a), and computations (panel b). Panel c shows the measured (grey circles) and computed (filled black circles) time lags, normalised with a representative bound ig-wave period, between the wave envelope and bound ig-waves.

\tilde{H}_{m0}^+ are larger than measured \tilde{H}_{m0}^- , especially for $x > 25$ m where the difference is largest. Computed \tilde{H}_{m0}^+ are in agreement with observation for $x > 22$ m, whereas they are under predicted for $x < 22$ m. The \tilde{H}_{m0}^- is over predicted throughout the domain, but the overall pattern and magnitude is in reasonable agreement with the measurements. To identify the cause of the under prediction of \tilde{H}_{m0}^- for $x < 22$ m, we compare the results with the target bound wave height, which is computed as the integral of the theoretical bound wave energies over the ig-frequency range, based on the incident free-wave components. To compare the target bound wave height with the most seaward located prediction of \tilde{H}_{m0}^+ , we assume that for $x < 10$ m the amplitude increase of the incoming ig-waves is in the order of Green's law (which is in agreement with the mild amplitude increase observed for $x < 20$ m). The resulting target bound wave height at $x = 9$ m is of similar magnitude as the predicted \tilde{H}_{m0}^+ , whereas it is smaller than the measured \tilde{H}_{m0}^+ at this position. This is in accordance with Battjes et al. (2004), who observed that the measured incident \tilde{H}_{m0}^+ is larger than the equilibrium bound wave height. Discrepancies between model results and the measurements are therefore related to differences between the wave forcing in the flume and in the numerical model. A possible explanation is that, in the flume, the wavemaker generated some (spurious) free-wave energy at ig-wave frequencies, for example, due to re-reflections of outgoing ig-waves.

The previous analysis was restricted to the total ig-wave band ($0.1f_p < f \leq 0.5f_p$). Now we consider the incoming and outgoing ig-wave heights for two separate frequency bands, which range between the ig-frequency limits with a fixed width of 0.06Hz. For the higher frequencies (Fig. 9c), the growth of incoming ig-waves is relatively strong and they are more energetic than the outgoing ig-waves. In contrast, for lower frequencies the incoming ig-waves are less energetic (Fig. 9b), compared to the outgoing ig-waves, and have a smaller growth rate compared to their counterparts at higher frequencies. Predicted wave heights are in agreement with the measurements for both frequency bands, although \tilde{H}_{m0}^+ is under and \tilde{H}_{m0}^- is over predicted for the lower frequency band.

Similar to the previous laboratory case we investigate the influence of the roughness coefficient for a coefficient ranging $d_r = 0.001 - 0.02m$. Again, the roughness coefficient has a small

influence on the magnitude of short waves (Fig. 8) and incoming ig-waves, whereas it has a significant influence on the outgoing ig-wave height (Fig. 9a). The influence of the roughness coefficient is most pronounced for ig-waves with relatively low frequencies (Fig. 9b).

It is well established that in waters of constant depth the wave envelope and bound ig-waves are in equilibrium and out of phase with one-another (e.g. Longuet-Higgins and Stewart, 1960). However, as waves propagate over regions with varying depths, a phase shift away from the 180° equilibrium difference develops as the bound waves lag behind the wave envelope (e.g. Janssen et al., 2003, and references therein). This can be illustrated using a cross-correlation analysis, which determines the relation between short-wave envelope and ig-waves. This technique has been applied to the Boers data set by several authors (e.g. Janssen et al., 2003; Torres-Freyermuth et al., 2010) to analyse the propagation and reflection of ig-waves.

The normalised cross-correlation function between two real signals $V(t)$ and $Y(t)$ is defined as

$$R_{VY}(\tau) = \frac{\langle V(t)Y(t+\tau) \rangle}{\sigma_V \sigma_Y}, \quad (10)$$

where τ is a time shift and σ_V and σ_Y are standard deviations of $V(t)$ and $Y(t)$, respectively. We define the short-wave envelope as the absolute value of (Janssen et al., 2003)

$$A(t) = \left| \zeta'(t) + i\mathcal{H}\{\zeta'(t)\} \right|_{lp}, \quad (11)$$

where $\mathcal{H}\{\dots\}$ is the Hilbert transform operator and $|\dots|_{lp}$ denotes a low pass filter operation ($f < 0.5f_p$).

Here, we evaluate the cross-correlation between the squared wave envelope and ig-wave surface elevation signal for the measurements and the model predictions. Fig. 10 shows the measured (panel a) and computed (panel b) cross-correlation function. In the measurements, a clear trough of negative correlation is present around zero time lags for $x < 30$ m, consistent with the theory of Longuet-Higgins and Stewart (1962), which predicts a bound ig-wave which is out of phase with the wave groups. For $x > 25$ m the correlation increases as the short waves are breaking and further shoreward ($x > 30$ m) the correlation is eventually reversed. This positive correlation is associated with the fact that ig-waves modulate the total water depth (Janssen et al., 2003), as the presence of an ig-wave crest increases the water depth whereas an ig-wave trough decreases the water depth. This allows depth-limited short waves to enter shallow water on the crest of an ig-wave, which results in a positive correlation. A second trough of negative correlation is present at greater time lags, which is linked to the reflected ig-wave (e.g. Janssen et al., 2003). Close to the wavemaker ($x = 5$ m) the minimum value of correlation that is associated with an incoming bound ig-wave is located at $\tau = 0s$, whereas closer to the shore the minimum value is located at increased time lags. This is further illustrated in Fig. 10c, which shows the time lag, normalised with a representative bound wave period $T_b (= 1/0.3f_p)$, of the minimum correlation value between $-5s < \tau < 5s$ (which corresponds to the incoming bound ig-wave) up to the location of the second breaker bar ($x \approx 30$ m). The measured normalised phase lag increases significantly for $x > 20$ m and reaches a value of ≈ 0.4 for $x > 27$ m, which corresponds to a phase difference of 36° between the wave envelope and a representative bound wave. Model predictions agree with the measurements, both in a qualitative manner (Fig. 10a and b) and a quantitative manner (Fig. 10c).

6. Discussion

The overall good correspondence between model results and measurements found in this study demonstrates that SWASH – which is essentially an intermediate approach between RANS and phase-averaged models – is able to resolve the cross-shore evolution of

ig-waves. SWASH accounts for the dominant processes that affect the energy balance at the ig-frequencies: the nonlinear energy exchange with the high-frequency waves, and the loss of energy due to friction and ig-wave breaking. The energy exchange with the hf-waves outside the surf zone is best represented in the model, as it is an intrinsic property of the governing equations. However, the accuracy of the modelled nonlinear interactions depends on the spatial resolution that is used (see e.g. Fig. B.1). On the other hand, bottom friction and (ig-wave) breaking are parametrized and with that model performance depends on how sensitive predictions are to (small) errors in the modelled dissipation related to these processes.

In this study predictions of the incoming wave field proved to be insensitive to variations in the bottom friction (by means of the roughness coefficient). In contrast, under (mildly) reflective wave conditions the outgoing ig-wave heights are sensitive to the bottom friction. In such cases, an accurate prediction of the outgoing ig-wave field requires the calibration of the roughness coefficient. Although a different friction formulation might reduce model sensitivity, it is unlikely that the need to calibrate the friction coefficient can be avoided without taking the effect of enhanced turbulence due to wave breaking into account (Feddersen et al., 2003).

Depth-induced wave breaking of the short waves is well resolved within SWASH as the relatively simple model used (bore dissipation with an enforced hydrostatic pressure distribution) is able to resolve the evolution of bulk wave parameters and wave spectra, including nonlinear wave-interactions, in high-detail throughout the surf zone (e.g. Smit et al., 2014). This gives confidence that SWASH accounts for the energy exchange between ig- and hf-waves in the surf zone. Moreover, the present study shows that SWASH captures the bulk energy dissipation of a breaking ig-wave. However, for such dissipative ig-wave conditions errors in predicted outgoing ig-wave heights are large, because the relatively small outgoing energies are sensitive to minor errors in the predicted bulk energy dissipation. Nonetheless, the model has a good skill in predicting the total ig-wave heights demonstrating that the low skill regarding the outgoing ig-waves does not inhibit the use of SWASH for the prediction of ig-waves.

The primary advantage of SWASH compared to RANS models is that the accuracy of predicted bulk wave parameters (including sea, swell and ig-contributions) is comparable, whereas the computational effort is much smaller. For example, the agreement with observed (ig-) wave heights for the Boers experiment (§5) is similar to the results of Torres-Freyermuth et al. (2010), who used a RANS model with 82 cells in the vertical, as opposed to two vertical layers used here, to reproduce this experiment. Naturally, if more detail with regard to the vertical structure is required, for instance to capture the wave-induced cross-shore circulation, SWASH may be employed with a finer vertical resolution (at larger computational costs). However, if only bulk parameters are of interest, the present approach forms an attractive alternative. Moreover, the non-hydrostatic approach is more flexible compared to Boussinesq-type models, which operate on a similar intermediate scale, as it can flexibly adapt itself to allow for an optimum balance between accuracy and computational effort.

Nevertheless, the prediction of ig-wave conditions in a two-dimensional surf zone, for routine applications, will likely remain in the class of models that combine a wave driver with the nonlinear shallow water equations. Such models, although more approximate, remain an order of magnitude faster as they do not resolve individual waves, but calculate on the wave-group scale. On the other hand, the use of linear wave theory for the evolution of the short waves and the absence of phase information implies that in regions where the waves are strongly nonlinear, or where reflection and/or diffraction (e.g. a harbour) are important, the present approach is preferable to the phase-averaged approach. We stress that there are no fundamental barriers to apply SWASH to two-dimensional ig-wave propagation cases. For instance, when the calculations are performed on present-day large-scale multi-processor machines (with O(100) processors),

the application of the present model to study ig-wave conditions in, for example, a large harbour, for select engineering (e.g. calculating extreme conditions) or scientific purposes, is viable.

7. Conclusions

In the present study we considered the modelling of ig-wave dynamics using the non-hydrostatic model SWASH. Hereto we extended SWASH with a second-order weakly-reflective wavemaker, based on weakly nonlinear wave theory, in order to include the incident (bound) ig-wave contributions. Model results were compared with flume observations of the nearshore transformation of ig-waves. Our results demonstrate that SWASH is able to reproduce the phenomena commonly associated with the evolution of ig-waves in the nearshore, including the shoaling of bound ig-waves, shoreline reflections, the phase lag between the wave envelope and the incoming ig-waves, nonlinear (self-self) interactions and the occurrence of ig-wave breaking. In particular, our analysis shows that the total and incoming ig-wave heights are well predicted. Errors in predicted outgoing ig-wave heights are larger compared to the total and incoming ig-wave height, and are found to be sensitive to the roughness coefficient (which controls the dissipation due to bottom friction) and to the location of incipient short-wave breaking (which is controlled by the breaking threshold). Model results further indicate that bottom friction has a marginal influence on the incoming wave field and only affects the magnitude of outgoing ig-waves in case of (mildly) reflective ig-wave conditions. This study suggests that SWASH can be a valuable tool, for engineering and scientific purposes, to study the evolution of cross-shore propagating ig-waves.

Acknowledgements

The authors thank Ap van Dongeren for providing the data of the bichromatic laboratory experiments and for the code of the signal decomposition tool. The investigations were (in part) supported by the Division for Earth and Life Sciences (ALW) with financial aid from the Netherlands Organisation for Scientific Research (NWO). We thank the anonymous reviewer whose comments improved this paper.

Appendix A. Second-order boundary condition

To include the ig-response into our boundary signal, we make use of weakly nonlinear, second-order, finite-depth theory (e.g. Hasselmann, 1962; Longuet-Higgins and Stewart, 1960). Herein the wave field is composed of first-order, or primary waves that corresponds to the free wave response (single summation in Eq. (6)), and a small second order correction that is associated with the bound waves (double summation in Eq. (6)). Here, we estimate the amplitude of the second order response, due to the primary waves at f_m and f_n , following Hasselmann (1962)

$$a_{nm} = D_{nm} a_m a_n, \quad (\text{A.1})$$

where a_{nm} is the amplitude of a bound wave component, a_n and a_m denote the amplitudes of the associated primary waves, and D_{nm} is the interaction coefficient. In this study we are primarily interested in the difference interactions, with difference frequency $f_{nm} = f_m - f_n$ and difference wave number $k_{nm} = k_m - k_n$, for which the interaction coefficient can be expressed as

$$D_{nm} = -\frac{gk_n k_m}{2\omega_n \omega_m} + \frac{\omega_n^2 - \omega_n \omega_m + \omega_m^2}{2g} - C \frac{g(\omega_n - \omega_m)}{\omega_n \omega_m [gk_{nm} \tanh(k_{nm}d) - (\omega_n - \omega_m)^2]}, \quad (\text{A.2})$$

where $\omega (= 2\pi f)$ is the radial frequency and coefficient C is defined as

$$C = (\omega_n - \omega_m) \left(\frac{(\omega_n \omega_m)^2}{g^2} + k_n k_m \right) - \frac{1}{2} \left(\frac{\omega_n k_m^2}{\cosh^2(k_m d)} - \frac{\omega_m k_n^2}{\cosh^2(k_n d)} \right). \quad (\text{A.3})$$

Because SWASH is forced by means of the horizontal particle velocity, the free surface amplitudes need to be related to the horizontal velocity amplitudes. In principle, this can be done using second-order theory. However, because in this study the long wave response is generally in shallow water ($k_{nm}d \ll 1$), a good approximation of the depth averaged second-order velocity amplitude \hat{u}_{nm} follows from mass conservation in combination with the assumption that bound ig-waves are progressive and of constant form,

$$\hat{u}_{nm} = \frac{c_g}{d} a_{nm}. \quad (\text{A.4})$$

where c_g is the group velocity which is expressed as $c_g = 2\pi f_b / k_{nm}$. This form is easier to implement and more efficient to compute compared to the full second-order theory. The above boundary condition, valid for unidirectional waves perpendicular to the boundary, can be extended to short-crested waves (directional seas) as the original interaction coefficient of Hasselmann (1962) puts no restriction on wave directions.

The interaction coefficient is derived with the assumption of weak nonlinearity, therefore, the above boundary condition is only valid for small wave amplitudes $a/d \ll 1$. Furthermore, the assumption of a depth averaged second-order velocity amplitude requires $k_{nm}d \ll 1$. These considerations imply that the proposed boundary condition cannot be used in the surf zone ($a/d < 1$) and in deep water ($k_{nm}d > 1$). Nevertheless, for most practical applications, including the simulations considered in this study, the boundary will be located in intermediate water depths where these limitations are not met. Furthermore, in deep water the second-order response is small and can – to a good approximation – be neglected. In such case, a boundary condition based on linear wave theory is likely sufficient.

Appendix B. SWASH second-order response

To verify the second-order boundary condition, and to investigate the sensitivity with regard to the vertical resolution, we compare the model response with the classical finite depth solution of Longuet-Higgins and Stewart (1960). Here we consider a situation where a bound ig-wave is forced by, and in equilibrium with, two free waves which propagate over a flat bottom. The accuracy with which the bound-solution is reproduced by SWASH is likely related to the number

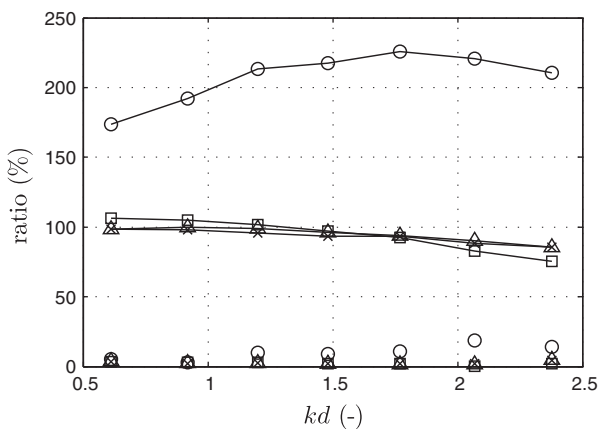


Fig. B.1. The ratio of the numerical spurious free and the analytical bound energy (markers) and ratio of the numerical and analytical bound energy (marked lines), for a simulation with 1 (circles), 2 (squares), 3 (triangles) and 4 (crosses) vertical layers.

of vertical layers, as the dispersive and nonlinear properties of SWASH improve with an increased number of layers. Furthermore, at low resolutions a spurious free wave with the same frequency as the bound ig-wave might be generated. Such a spurious free wave is most pronounced when the second order response is not incorporated. In this case a spurious free wave is generated, out of phase with but of equal amplitude as the bound wave, which exactly cancels the bound wave at the wavemaker. Hence, inclusion of the second-order response is vital to avoid generating artificial free-energy at the ig-frequencies. However, because SWASH will not exactly reproduce second-order theory some spurious free-energy is still generated, even when the ig-waves are included at the boundary.

To properly estimate the bound energy which is generated, and to investigate the magnitude of the spurious free wave, we need to decompose the energy associated with the low-frequency motion into bound and free energy. Given that the free and bound waves have identical frequencies, this decomposition cannot be done in the wave number domain. Instead, we will perform the decomposition in the wave number domain as a bound wave and its spurious counterpart have different wave numbers (the bound wave number is equal to the difference wave number and the free wave number follows from the difference frequency and the linear dispersion relationship). We estimate their respective energies using a spatial Fourier transform, which results in the complex wave amplitude a_k at wave numbers k . In this manner we can estimate the energy associated with the free or bound wave components (\tilde{E}_f and \tilde{E}_b , respectively) with

$$\tilde{E}_f = \sum_{\delta k_f} \frac{1}{2} a_k a_k^*, \quad \tilde{E}_b = \sum_{\delta k_b} \frac{1}{2} a_k a_k^*, \quad (16)$$

where $*$ denotes the complex conjugate and $\delta k_{b/f}$ denote the wave number range around the free (subscript f) or bound (subscript b) wave numbers.

Model results and analytical solutions are analysed for fixed free-wave amplitudes ($a_1 = a_2 = 0.01\text{m}$), fixed free-wave frequencies ($f_1 = 0.10\text{Hz}$ and $f_2 = 0.11\text{Hz}$) and varying still water depths which range from 7.5 to 65 m. This range of still water depths results in a minimum and maximum kd value of 0.5 and 2.5, respectively. Numerical simulations are performed with one to four vertical layers and a grid resolution of $\Delta x < \lambda/100$, where λ is the wave length of the second free wave component (which corresponds to the shortest wave length). A radiation condition, in combination with a sponge layer, was employed to minimise wave reflections at the outlet of the domain. The roughness coefficient and vertical viscosity are equal to zero to prevent wave damping. Numerical and analytical surface elevations were outputted for a domain length of L , such that the signals contain at least 75 bound waves, with a resolution of Δx . A visual inspection of the computed complex amplitudes showed that with a wave number range of $\delta k_{b/f} = k_{b/f} \pm 5\Delta k$, where $\Delta k = 1/L$, most bound and spurious wave energies were included in the estimation of $\tilde{E}_{f/b}$.

The second-order boundary condition successfully suppresses the generation of spurious free ig-waves, although some spurious energy is present for simulations with one vertical layer (Fig. 1). Predicted and analytical bound ig-wave energies are in good agreement for two to four vertical layers, whereas it is over predicted by the one layer model. This indicates that the response of the depth-averaged model is different than the response of a multi-layer model. A multi-layer model under predicts the bound wave height for greater kd values, which is largest in case of two vertical layers. Furthermore, with two vertical layers the bound energies are overestimated for lower kd values. Nevertheless, numerical results are in agreement with the analytical solutions. These results indicate that at least two vertical layers are required to predict a bound ig-wave response which is in accordance with the classical finite depth theory of Longuet-Higgins and Stewart (1960).

References

- Battjes, J.A., Bakkenes, H.J., Janssen, T.T., van Dongeren, A.R., 2004. Shoaling of subharmonic gravity waves. *J. Geophys. Res. Oceans* 109.
- Boers, M., 1996. Simulation of a surf zone with a barred beach. Report 1. Wave heights and wave breaking. Technical Report. Delft University of Technology.
- Bowers, E.C., 1977. Harbour resonance due to set-down beneath wave groups. *J. Fluid Mech.* 79, 71–92.
- Bromirski, P.D., Sergienko, O.V., MacAyeal, D.R., 2010. Transoceanic infragravity waves impacting Antarctic ice shelves. *Geophys. Res. Lett.* 37.
- Cienfuegos, R., Barthlemy, E., Bonneton, P., 2010. Wave-breaking model for Boussinesq-type equations including roller effects in the mass conservation equation. *J. Waterw. Port Coast. Ocean Eng.* 136, 10–26.
- Fedderson, F., Gallagher, E., Guza, R., Elgar, S., 2003. The drag coefficient, bottom roughness, and wave-breaking in the nearshore. *Coast. Eng.* 48, 189–195.
- Hasselmann, K., 1962. On the non-linear energy transfer in a gravity-wave spectrum Part 1. General theory. *J. Fluid Mech.* 12, 481–500.
- Henderson, S.M., Bowen, A.J., 2002. Observations of surf beat forcing and dissipation. *J. Geophys. Res. Oceans* 107.
- Henderson, S.M., Guza, R.T., Elgar, S., Herbers, T.H.C., Bowen, A.J., 2006. Nonlinear generation and loss of infragravity wave energy. *J. Geophys. Res. Oceans* 111.
- Holthuijsen, L.H., 2007. *Waves in Oceanic and Coastal Waters*. Cambridge University Press.
- Janssen, T.T., Battjes, J.A., van Dongeren, A.R., 2003. Long waves induced by short-wave groups over a sloping bottom. *J. Geophys. Res. Oceans* 108.
- Kennedy, A., Chen, Q., Kirby, J., Dalrymple, R., 2000. Boussinesq modeling of wave transformation, breaking, and runup. i: 1D. *J. Waterw. Port Coast. Ocean Eng.* 126, 39–47.
- Lamb, H., 1932. *Hydrodynamics*. Dover, New York.
- Lara, J.L., Ruju, A., Losada, I.J., 2011. Reynolds averaged Navier–Stokes modelling of long waves induced by a transient wave group on a beach. *J. Proc. R. Soc. A Math. Phys. Eng. Sci.* 467, 1215–1242.
- Lin, P., Liu, P.L.F., 1998. A numerical study of breaking waves in the surf zone. *J. Fluid Mech.* 359, 371–388.
- List, J.H., 1992. A model for the generation of two-dimensional surf beat. *J. Geophys. Res. Oceans* 97.
- Longuet-Higgins, M.S., Stewart, R.W., 1960. Changes in the form of short gravity waves on long waves and tidal currents. *J. Fluid Mech.* 8, 565–583.
- Longuet-Higgins, M.S., Stewart, R.W., 1962. Radiation stress and mass transport in gravity waves, with application to 'surf beats'. *J. Fluid Mech.* 13, 481–504.
- Longuet-Higgins, M.S., Stewart, R.W., 1964. Radiation stresses in water waves; a physical discussion, with applications. *Deep-Sea Res.* 11, 529–562.
- Ma, G., Shi, F., Kirby, J.T., 2012. Shock-capturing non-hydrostatic model for fully dispersive surface wave processes. *Ocean Model.* 43–44, 22–35.
- Madsen, P.A., Sørensen, O.R., 1993. Bound waves and triad interactions in shallow water. *Ocean Eng.* 20, 359–388.
- Madsen, P.A., Murray, R., Sørensen, O.R., 1991. A new form of the Boussinesq equations with improved linear dispersion characteristics. *Coast. Eng.* 15, 371–388.
- Madsen, P.A., Sørensen, O., Schäffer, H., 1997. Surf zone dynamics simulated by a Boussinesq type model. Part II: surf beat and swash oscillations for wave groups and irregular waves. *Coast. Eng.* 32, 289–319.
- Masselink, G., 1995. Group bound long waves as a source of infragravity energy in the surf zone. *Cont. Shelf Res.* 15, 1525–1547.
- Naciri, M., Buchner, B., Bunnik, B., Huijsmans, R., Andrews, R., 2004. Low frequency motions of LNG carriers in shallow water. *Proceedings Offshore Mechanics and Arctic Engineering Conference*.
- Nwogu, O., 1993. Alternative form of Boussinesq equations for nearshore wave propagation. *J. Waterw. Port Coast. Ocean Eng.* 119, 618–638.
- Peregrine, D.H., 1967. Long waves on a beach. *J. Fluid Mech.* 27, 815–827.
- Pomeroy, A., Lowe, R., Symonds, G., van Dongeren, A.R., Moore, C., 2012. The dynamics of infragravity wave transformation over a fringing reef. *J. Geophys. Res. Oceans* 117.
- Reniers, A.J.H.M., Van Dongeren, A.R., Battjes, J.A., Thornton, E.B., 2002. Linear modeling of infragravity waves during Delilah. *J. Geophys. Res. Oceans* 107.
- Reniers, A.J.H.M., MacMahan, J.H., Thornton, E.B., Stanton, T.P., 2006. Modelling infragravity motions on a rip-channel beach. *Coast. Eng.* 53, 209–222.
- Reniers, A.J.H.M., Groenewegen, M.J., Ewans, K.C., Masterton, S., Stelling, G.S., Meek, J., 2010. Estimation of infragravity waves at intermediate water depth. *Coast. Eng.* 57, 52–61.
- Roelvink, D., Reniers, A.J.H.M., Van Dongeren, A.R., Thiel, Van, de Vries, J.S.M., McCall, R., Lescinski, J., 2009. Modelling storm impacts on beaches, dunes and barrier islands. *Coast. Eng.* 56, 1133–1152.
- Ruju, A., Lara, J.L., Losada, I.J., 2012. Radiation stress and low-frequency energy balance within the surf zone: a numerical approach. *Coast. Eng.* 68, 44–55.
- Schäffer, H.A., Madsen, P.A., Deigaard, R., 1993. A Boussinesq model for waves breaking in shallow water. *Coast. Eng.* 20, 185–202.
- Smit, P.B., Zijlema, M., Stelling, G.S., 2013. Depth-induced wave breaking in a non-hydrostatic, near-shore wave model. *Coast. Eng.* 76, 1–16.
- Smit, P., Janssen, T., Holthuijsen, L., Smith, J., 2014. Non-hydrostatic modeling of surf zone wave dynamics. *Coast. Eng.* 83, 36–48 (ISSN 0378-3839), <http://dx.doi.org/10.1016/j.coastaleng.2013.09.005>.
- Stelling, G.S., Duijnmeijer, S.P.A., 2003. A staggered conservative scheme for every froude number in rapidly varied shallow water flows. *Int. J. Numer. Methods Fluids* 43, 1329–1354.
- Stelling, G.S., Zijlema, M., 2003. An accurate and efficient finite-difference algorithm for non-hydrostatic free-surface flow with application to wave propagation. *Int. J. Numer. Methods Fluids* 43, 1–23.
- Symonds, G., Huntley, D.A., Bowen, A.J., 1982. Two-dimensional surf beat: Long wave generation by a time-varying breakpoint. *J. Geophys. Res. Oceans* 87.
- Thomson, J., Elgar, S., Raubenheimer, B., Herbers, T.H.C., Guza, R.T., 2006. Tidal modulation of infragravity waves via nonlinear energy losses in the surfzone. *Geophys. Res. Lett.* 33.
- Tissier, M., Bonneton, P., Marche, F., Chazel, F., Lannes, D., 2012. A new approach to handle wave breaking in fully non-linear Boussinesq models. *Coast. Eng.* 67, 54–66.
- Tonelli, M., Petti, M., 2012. Shock-capturing Boussinesq model for irregular wave propagation. *Coast. Eng.* 61, 8–19.
- Torres-Freyermuth, A., Lara, J.L., Losada, I.J., 2010. Numerical modelling of short-and long-wave transformation on a barred beach. *Coast. Eng.* 57, 317–330.
- Van Dongeren, A.R., Reniers, A.J.H.M., Battjes, J.A., Svendsen, I.A., 2003. Numerical modeling of infragravity wave response during Delilah. *J. Geophys. Res. Oceans* 108.
- Van Dongeren, A.R., Battjes, J.A., Janssen, T.T., van Noorloos, J., Steenhauer, K., Steenbergen, G., Reniers, A.J.H.M., 2007. Shoaling and shoreline dissipation of low-frequency waves. *J. Geophys. Res. Oceans* 112.
- Van Dongeren, A.R., Lowe, R., Pomeroy, A., Trang, D.M., Roelvink, D., Symonds, G., Ranasinghe, R., 2013. Numerical modeling of low-frequency wave dynamics over a fringing coral reef. *Coast. Eng.* 73, 178–190.
- Van Noorloos, J., 2003. *Energy Transfer between Short Wave Groups and Bound Long Waves on a Plane Slope*. (MSc thesis) Delft University of Technology.
- van Thiel de Vries, J., van Gent, M., Walstra, D., Reniers, A., 2008. Analysis of dune erosion processes in large-scale flume experiments. *Coast. Eng.* 55, 1028–1040.
- Wei, G., Kirby, J.T., Grilli, S.T., Subramanya, R., 1995. A fully nonlinear Boussinesq model for surface waves. Part I. Highly nonlinear unsteady waves. *J. Fluid Mech.* 294, 71–92.
- Zijlema, M., Stelling, G.S., 2008. Efficient computation of surf zone waves using the nonlinear shallow water equations with non-hydrostatic pressure. *Coast. Eng.* 55, 780–790.
- Zijlema, M., Stelling, G.S., Smit, P.B., 2011. SWASH: an operational public domain code for simulating wave fields and rapidly varied flows in coastal waters. *Coast. Eng.* 58, 992–1012.